agronomy

MDPI

Article

A Novel Non-Invasive Method for Real-Time Monitoring of Plant Water Status Based on Xylem Electrical Conductivity

Junchao Huang *, Jiahui Huang, Junjie Gu and Xuzhuang Yao

College of Optical, Mechanical and Electrical Engineering, Zhejiang A & F University, Hangzhou 311300, China
* Correspondence: jc_huang@zju.edu.cn

Abstract

Non-invasive, real-time monitoring of plant water status is critical for precision agriculture and plant physiology. However, existing methods often lack continuous in situ measurement capability or are limited by temporal resolution. This paper proposes a novel non-invasive method based on xylem electrical conductivity, inspired by industrial non-contact fluid measurement. As a ground-based complement to remote sensing, this approach demonstrates the feasibility of online, in situ, and non-invasive monitoring of water stress in grapevine stems under controlled laboratory conditions. The industrial C^4D sensing system is adaptively modified into a specialized Plant-C^4D sensor with an array-based design for batch signal acquisition. To validate the electrical response to water loss, a gravimetric natural dehydration experiment was conducted, demonstrating a clear correlation between electrical signals and water content changes in detached stem samples. Full-day dynamic experiments are conducted under three conditions: normal water supply, varying water stress, and plant inactivation. Sensitive characteristic parameters are extracted through signal analysis, and a pattern recognition framework is established to eliminate environmental interference and suppress individual differences. Experimental results on 24 plant samples (Shine Muscat) show that the method accurately discriminates viable from inactivated plants with an accuracy of 91.67% (22/24 correct). Furthermore, the Fuzzy C-Means (FCM) clustering algorithm successfully quantifies the severity of water stress in viable plants, yielding results consistent with actual water supply conditions. While these findings demonstrate the capability of Plant-C^4D sensor to capture stem water status-related information, the current results do not establish full physiological validation, warranting further exploration with in vivo experiments.

Keywords: water status; xylem electrical conductivity; non-invasive; water stress; viable/inactivated sample identify

Academic Editors: Francisco Montoya and Susana Ferreira

Received: 14 June 2026
Revised: 22 July 2026
Accepted: 25 July 2026
Published: 27 July 2026

1. Introduction

The water physiological status of woody plants is a core indicator characterizing the plant's water balance, metabolic activity, and stress response characteristics [1,2]. It serves as a crucial basis for optimizing precision irrigation, preventing and controlling drought in orchards, and quantitatively assessing plant drought stress [3,4]. Existing studies have confirmed that monitoring the stem water status (especially the stem hydration level) of woody plants and its dynamic variation patterns can stably and reliably reflect the overall water physiological status of the plant. Although leaves are the active sites of transpiration, the stem serves as a crucial hydraulic capacitor and transport pathway. Therefore, monitoring stem water status provides a comprehensive metric of plant water balance, reflecting the dynamic equilibrium between root water uptake and leaf transpiration demand [5–9].

In the field of plant water status monitoring, remote sensing technologies have established themselves as the paramount approach for large-scale observation [3,10–19]. By the advanced technology such as hyperspectral imaging [10,11], thermal infrared [11,12], UVA [10,13,14] and machine learning [15,16], remote sensing enables the rapid, non-contact acquisition of spatiotemporal data across vast landscapes [3,10–19]. Canopy water content and stress levels over large areas can be effectively measured by these methods [10–15]. However, despite these macroscopic capabilities, remote sensing operates fundamentally on surface reflectance and emission [3,10,19]. It faces a physical "blind spot" regarding the internal hydrodynamics of woody plants: optical and thermal signals cannot penetrate the opaque bark to sense the real-time moisture status within the stem—the critical conduit of water transport [19]. Furthermore, visible symptoms detectable from the air often manifest only after the plant has already undergone significant water physiological stress [17,18]. Traditionally, direct contact methods like psychrometry serve as the "gold standard" for measuring internal water potential [20]. Yet, these invasive techniques inevitably cause wounding to the stem, potentially altering local hydraulic conductivity. In this context, electrical detection offers a scientific avenue to explore internal stem moisture without physical intrusion. Therefore, rather than competing with remote sensing, electrical detection methods serve as a necessary, complementary "ground-truth" mechanism [21–24]. By providing direct, in situ quantification of internal stem water, electrical methods fill the vertical observational gap left by remote sensing, offering the precise, subsurface data needed to validate and calibrate macro-scale remote sensing models.

Electrical detection method employs electrical sensors to collect parameters such as equivalent resistance, dielectric properties, or electrical impedance [21–24] from the targeted plant tissues. Based on impedance–physiological characteristic correlation models, this method inverts the internal water content and physiological status of the tissue. Typical techniques include electrical impedance spectroscopy [25–29], electrical capacitance tomography [30–33], and flexible sensors [29,34–38]. Traditional electrical methods work well on thin-skinned, high-water-content tissues like leaves, fruits, and herbaceous stems [34–38]. However, leaves and fruits of woody plants are highly seasonal and provide only localized water information. The stem better represents overall plant water status, but its thick insulating bark blocks electrical signals [21–24]. To obtain internal electrical information from the stem, traditional approaches must employ invasive probe sensors [21,28,29]. This disrupts structural integrity and causes scar tissue and electrode contact failure over time, precluding long-term stable monitoring. More critically, invasive probes inevitably sever xylem vessels [39] or trigger wound responses (e.g., tyloses formation or gel occlusion [40]), thereby disrupting the continuity of the water column and altering local water potential gradients [41]. Consequently, existing methods fail to capture the continuous, high-temporal-resolution hydration dynamics—specifically the rapid fluctuations in stem hydraulic conductance—essential for understanding plant water physiology. Hence, a non-invasive, online technology for woody plant stems that enables real-time water stress identification without interfering with growth is urgently needed—to support both precision agriculture and plant water physiology research.

High-frequency excitation penetrates leaf cuticles for non-destructive water detection [29], but woody stem bark is ~1000× thicker (mm vs. 1–5 μm) [2]. Direct application would require excessive frequencies, altering electrolyte and dielectric models [1,2,42] and invalidating impedance measurements. Thus, high-frequency methods cannot be directly transferred to woody stems. However, the principle of penetrating insulating layers via high frequencies is central to mature Capacitively Coupled Contactless Conductivity Detection (C^4D) technology [43–47]. In C^4D, high-frequency AC on electrodes outside insulated pipes detects internal fluid parameters via coupling capacitance [47,48]. Since industrial applications also face thick insulation—where pure high-frequency excitation distorts models—mature C^4D structures and signal processing can be extended to detect stem conductivity [47–50]. Furthermore, xylem vessels are analogous to insulated pipes, making industrial multiphase flow methods applicable to plant water status monitoring.

To address the above challenges, this paper draws on industrial non-contact fluid measurement to propose a novel non-invasive method for real-time monitoring of woody plant water status based on xylem electrical conductivity, serving as a ground-based complement to remote sensing observations. The industrial C^4D sensing system is adaptively modified for plant-specific characteristics to construct a specialized Plant-C^4D sensor, and an array-based measurement system is designed for batch signal acquisition from multiple samples. Through full-day dynamic experiments under different water supply conditions, sensitive characteristic parameters are extracted and, drawing on industrial multiphase flow pattern identification theory, a pattern recognition framework is established. This framework eliminates environmental interference and suppresses individual differences to achieve accurate discrimination between viable and inactivated plants, with the Fuzzy C-Means clustering algorithm further introduced to quantitatively assess water stress severity in viable plants.

2. Materials and Methods

2.1. Material

The experimental samples used were two-year-old grapevine branches of the variety Shine Muscat, grown at Zhejiang A&F University campus in Hangzhou, Zhejiang, China. A total of 30 plants were prepared in the experiment (6 plants suffered from non-experimental mortality or damage), all of which were under identical cultivation conditions before the experimental treatment. The samples selected for the experiment had similar heights and diameters, with heights controlled at 30 ± 5 cm and diameters at 8 ± 1 cm. Copper foil with a thickness of 0.5 mm was used as the electrode material, and PVA white glue (Deli Group Co.,Ltd. Zhejiang, China) was chosen as the adhesive.

2.2. Plant-C^4D Sensor

2.2.1. Principle of C^4D

Figure 1 provides a simplified description of the classical industrial C^4D principle and the challenges of expanding into plants.

As shown in Figure 1a, two metal ring electrodes are axially mounted on the outer side of the pipeline, serving as excitation and detection electrodes. An AC signal $U_{in} = A\sin\omega t$ is applied to the excitation electrode, which penetrates through the insulating pipe wall via the coupling capacitance C_{pipe} formed between the pipe wall and the fluid inside, carrying impedance information of the measured fluid R_{fluid}. This information emerges as an output current $I_{OUT} = \frac{U_{in}}{\frac{1}{j\omega C_{pipe}} + R_{fluid}}$ from the detection electrode, allowing for inference of the impedance characteristics of the measured fluid by I_{OUT}, for more detailed information, please refer to reference [43,44]. When extended to plant monitoring, this mechanism can be directly applied to penetrate the outer insulating plant bark and obtain information about changes in xylem moisture content, $C_{pipe} \rightarrow C_{bark}$, $R_{fluid} \rightarrow R_{xylem}$.

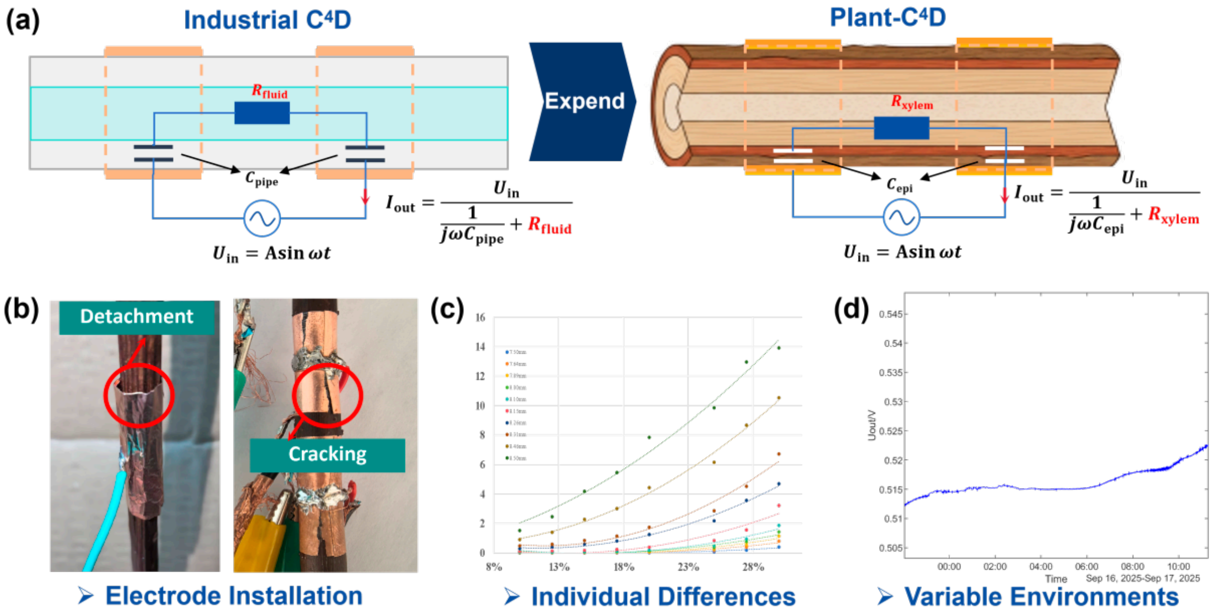

Figure 1. C^4D Principle and challenges in plant expansion: (**a**) Principle of C^4D, (**b**) Challenge of electrode installation on plant stem, (**c**) Challenge of individual differences in test subjects, (**d**) challenge of variable environments during long detection periods.

However, several challenges must still be overcome to apply industrial C^4D technology to plant:

Challenge 1: Electrode Installation on Plant Stems

Unlike the standardized dimensions and smooth exteriors of industrial pipelines, plant stems have irregular shapes. Additionally, their diameters change due to physiological activities (water absorption, water loss, growth), making traditional ring-shaped electrodes unsuitable Figure 1b illustrates the issues with ring-shaped electrodes caused by diameter changes, including detachment (where the electrode falls off due to a decrease in stem diameter after installation) and cracking (where the electrode cracks due to an increase in stem diameter after installation). Radial electrodes also suffer from poor sensitivity and performance on small-diameter targets. Therefore, it is necessary to optimize the electrode structure to fit plant stems, ensuring stable attachment without harming the plant. Section 2.2.2 will primarily discuss this issue.

Challenge 2: Individual Differences in Test Subjects

Unlike the relatively consistent physical/chemical properties of industrial pipelines and their contents, plant samples exhibit individual differences. Their intrinsic impedance characteristics, including baseline moisture content and skin equivalent capacitance, vary. Thus, unlike industrial applications, standard calibration states cannot be used. Figure 1c illustrates the natural water loss experiments conducted on ten samples with varying diameters and initial moisture contents. As shown, although the trends are consistent, the output signal amplitudes differ due to individual variations. To maintain plant vitality, complete drying methods cannot be used to determine absolute moisture content. Therefore, signal processing techniques must be employed to extract physiological state-related information from relative changes in moisture content. Section 2.4 will focus on how algorithms can mitigate the impact of sample variability.

Challenge 3: Variable Environments during Long Detection Periods

Compared to controlled industrial environments, agricultural settings are complex and unpredictable, with plant physiological activities being much slower than industrial processes, requiring longer detection periods. This further amplifies environmental impacts on measurements, as illustrated by temperature-induced sensor drift in Figure 1d.

Therefore, sensors must incorporate technical solutions to compensate for measurement deviations caused by variable environmental conditions. The design of the detection system (Section 2.2.2) will address compensating for environmental influences.

The research process on pC^{4}D sensors, measurement systems, and identification algorithms will prioritize addressing these issues.

2.2.2. P-C^{4}D Sensor and Array Measurement System

(1) Sensor Electrodes: A semi-annular electrode structure was designed as shown below. This design ensures the measurement sensitivity of an annular electrode while incorporating the radial electrode's adaptability to changes in stem diameter, thereby overcoming Challenge 1.

The electrodes are fabricated from 0.5 mm thick copper foil bonded using PVA white glue. Shielded wires are used for the excitation electrode leads, whereas unshielded wires are employed for the detection electrode leads. The electrode length l is 10 mm, with a subtended angle Φ of 150 degrees (an error margin of approximately 10 degrees exists due to the non-perfectly cylindrical contour of the plant stems). The excitation and detection electrodes are mounted diametrically opposite to each other but are axially offset, the distance between the electrodes d is 10 mm. Figure 2 illustrates the structure of the sensor electrodes.

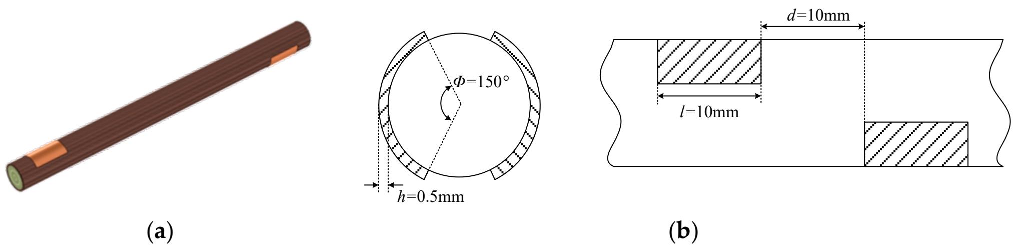

Figure 2. Sensor Electrodes: (**a**) Semi-annular electrode structure; (**b**) Electrode installation dimensions.

(2) Signal Processing Unit: The internal circuitry of the signal processing unit is illustrated in Figure 3. It primarily consists of a signal processing module, an analog-to-digital conversion (ADC) module, a signal generation module, a digital output module, a power management module, and a microprocessor. The signal processing module mainly comprises an I/V conversion circuit and an electrical impedance measurement circuit. The I/V conversion circuit transforms the output current into a voltage signal U_{out}. An RMS measurement circuit then obtains the root mean square value of U_{out}, i.e., U_o via full-wave rectification and low-pass filtering. The power management module distributes power from an external supply to the various circuits within the system. The ADC module samples the RMS voltage $U_o(t)$ and transmits them to a computer. The signal generation module provides AC excitation input for the AC-EX of the signal integration unit. The digital output module supplies electronic switch control signals S1~S8 to facilitate subsequent array measurements. The microprocessor handles data storage, signal generation control, and digital output control, and can be implemented using a microcontroller unit (MCU).

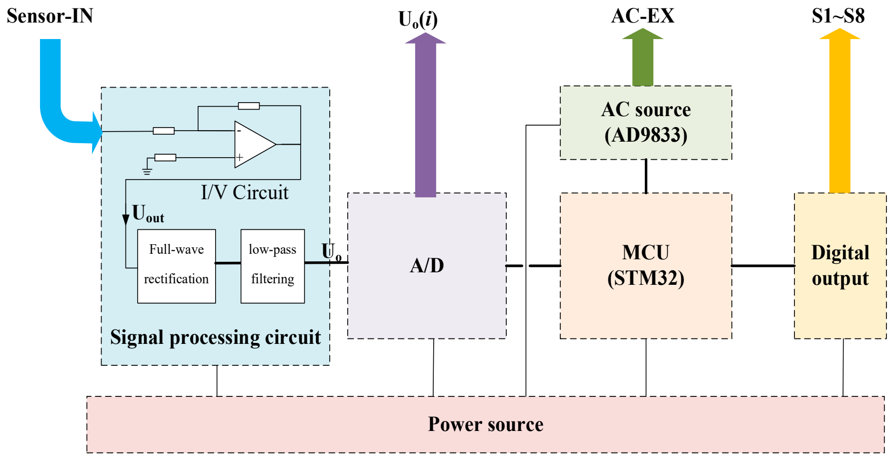

Figure 3. Internal circuit diagram of the data processing module.

(3) Array Measurement System: To achieve integrated applications, an array measurement system was established as depicted in Figure 4.

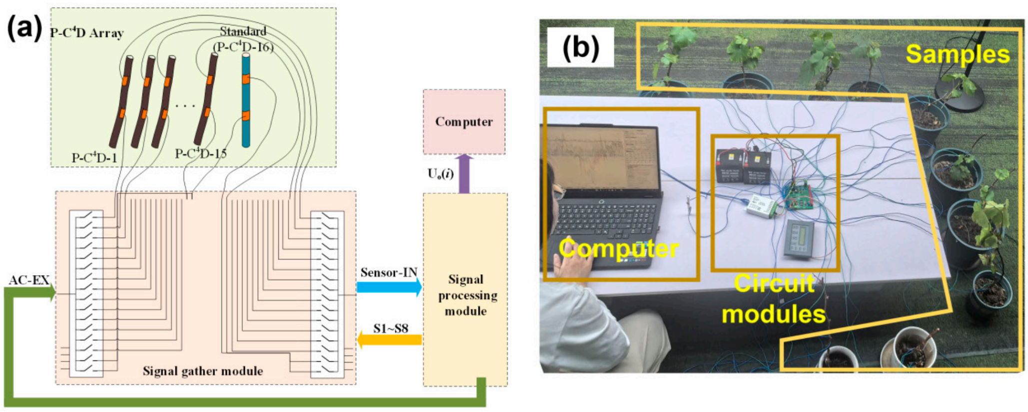

Figure 4. Array Measurement System prototype: (**a**) Structural diagram of the prototype; (**b**) Practical prototype.

This system dynamically collects electrical response signals from batches of plant samples exhibiting different typical water physiological states, facilitating bulk identification experiments and further practical application deployment. The prototype identification system comprises a P-C^{4}D Array, a signal acquisition module, a data processing module, and a computer.

During operation, multiple pairs of P-C^{4}D sensors (P-C^{4}D-1 to P-C^{4}D-15) are individually installed on the sample plants. Additionally, one pair of P-C^{4}D sensors (P-C^{4}D-16) is mounted on a standard reference sample, which consists of a sealed acrylic tube filled with a specially formulated electrolyte solution (possessing an equivalent conductivity matching that of the plant stems). This reference sensor serves to eliminate signal fluctuations caused by ambient temperature variations and circuit thermal drift. Collectively, these P-C^{4}D sensors form the P-C^{4}D array. Each sensor connects to the signal integration module via its respective excitation signal line (to the excitation interface) and detection signal line (to the detection interface). A single signal integration module supports simultaneous connection to up to 15 test samples. The raw measurement data from the signal integration module is routed to the signal processing module (i.e., the conductivity detection circuit designed in Figure 3).

2.3. Experimental Setup

Totally 48 experimental sets were conducted. Due to space limitations, the experiments were carried out in four batches. In each batch, 2–4 plant samples representing three different physiological states were selected: normal growth, water stress (subdivided into mild and severe stress based on the duration of irrigation cessation), and complete inactivation. The typical plant samples are shown in Figure 5.

(**a**) Normal growth (**b**) Water stress (**c**) Complete inactivation

Figure 5. The typical plant samples.

The parameters for the experimental procedures were set as follows:

Experimental Schedule: The experiments were conducted from 9:00 AM to 9:00 AM the following day across four dates: September 3 (Batch 1), 12 (Batch 2), 15 (Batch 3), and 18 (Batch 4), 2025.

Environmental Conditions: The experiments took place in a well-ventilated indoor environment. The air humidity was maintained at 50% ± 5%, and the temperature was controlled at 25 °C ± 1 °C using an air conditioner. The light intensity was set to 500 lx with a photoperiod of 12 h/12 h (light/dark).

Plant Samples: Two-year-old lignified branches of 'Shine Muscat' grapevines were used. The diameter of all samples was controlled at 8 mm ± 1 mm, and the plant height was maintained at 30 cm ± 5 cm. All samples were propagated from cuttings in February 2025. Samples in the normal growth state received no special treatment. For the water-stressed plants, irrigation was ceased 36–72 h prior to the start of the experiment and remained suspended until the experiment concluded. The completely inactivated samples were baked at 80 °C for 12 h, starting 24 h before the experiment began, to ensure complete inactivation. Due to the limited size of the oven, the inactivated samples were shorter, measuring approximately 15 cm in length.

Irrigation Strategy: The normal growth and completely inactivated samples followed the same irrigation strategy. Soil moisture content was measured using a soil moisture meter (Model Stevens Water—HydraProbe II) to serve as the baseline. At the beginning of the experiment, the soil moisture content was controlled at approximately 60%. Water was replenished at 20:00 to raise the moisture content to 70%. For the water-stressed samples, water was replenished only once at 20:00 to reach 70%.

Experimental Design: Initially, 30 plant specimens were prepared for the experiment. Due to unforeseen mortality and damage during the acclimatization period, the final sample size was reduced to n = 24. The experimental procedure involved two rounds of measurements on these same 24 plants to allow for a recovery period between stress treatments, resulting in a total of 48 measurement sets. However, to maintain statistical independence, the results presented in this study are based on the data from the primary experimental round (n = 24). A post hoc power analysis indicated that this sample size provides adequate statistical power ($1 - \beta = 0.86$) to detect significant effects at $\alpha = 0.05$.

2.4. State Identification Method

2.4.1. Environmental Noise Compensation

After extracting the conductivity output signals from each channel, the signal from the standard sample (P-C^4D-16, as shown in Figure 4a) is first utilized to eliminate temperature interference across all channels. To ensure this reference sample perfectly mirrors the thermal response of the actual plants, it is specifically engineered with identical geometry and electrode structure, and its electrolyte conductivity is adjusted to match the electrical baseline of the tested plants. Furthermore, it is co-located in the exact same testing environment.

Theoretically, since the stem hydration level within the measured region of the solidified standard sample remains constant, its electrical conductivity signal should be stable. Consequently, any observed fluctuations are entirely attributable to system thermal drift induced by circuit heating and ambient temperature variations. In this study, these fluctuations serve as a baseline for temperature compensation, thereby overcoming Challenge 3. The temperature compensation procedure is outlined as follows:

(1) Calculate the initial compensation sequence: using the following formula: $s_0(t) = U_{16,0}(t)/U_{16,0}(1)$, where $U_{16,0}(t)$ represents the raw signal of P-C^4D-16, and $U_{16,0}(1)$ denotes the output signal at the initial sampling point. By establishing the starting point as the relative zero reference for thermal drift, $s_0(t)$ physically represents the amplification factor drift at time t.

(2) Perform calibration compensation on each sampling point of the respective signals to obtain the compensated signals: $U_x(t) = U_{x,0}(t)s_0(t)$, where $U_{x,0}(t)$ represents the raw output signal of the P-C^4D-x sensor (x denotes the channel number of each P-C^4D sensor installed on a plant stem).

2.4.2. Viability Identification

To identify plant viability, this study proposes a viability rhythm correlation factor derived from cross-correlation calculations to characterize biological activity. The operational mechanism of the viability rhythm correlation factor is illustrated in Figure 6.

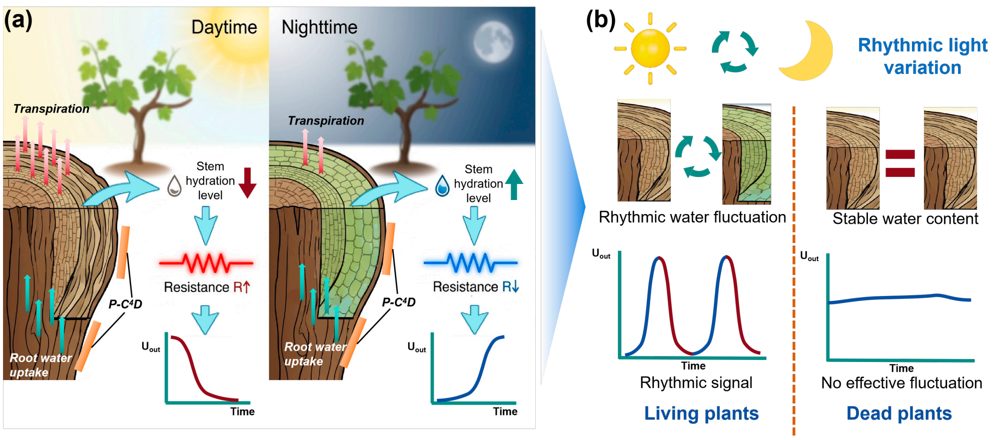

Figure 6. Detection mechanism of the viability rhythm correlation factor (plants and background elements in the figure were generated using AI [Nano Banana 2.0]): (**a**) Mechanism of daytime and nighttime stem resistance changes based on water status variations; (**b**) Mechanism driven by circadian rhythms.

Regardless of the presence or severity of stress, living plants consistently exhibit rhythms associated with light exposure. Its detection mechanism is listed in Table 1:

Table 1. Detection mechanism of daylight time and night time.

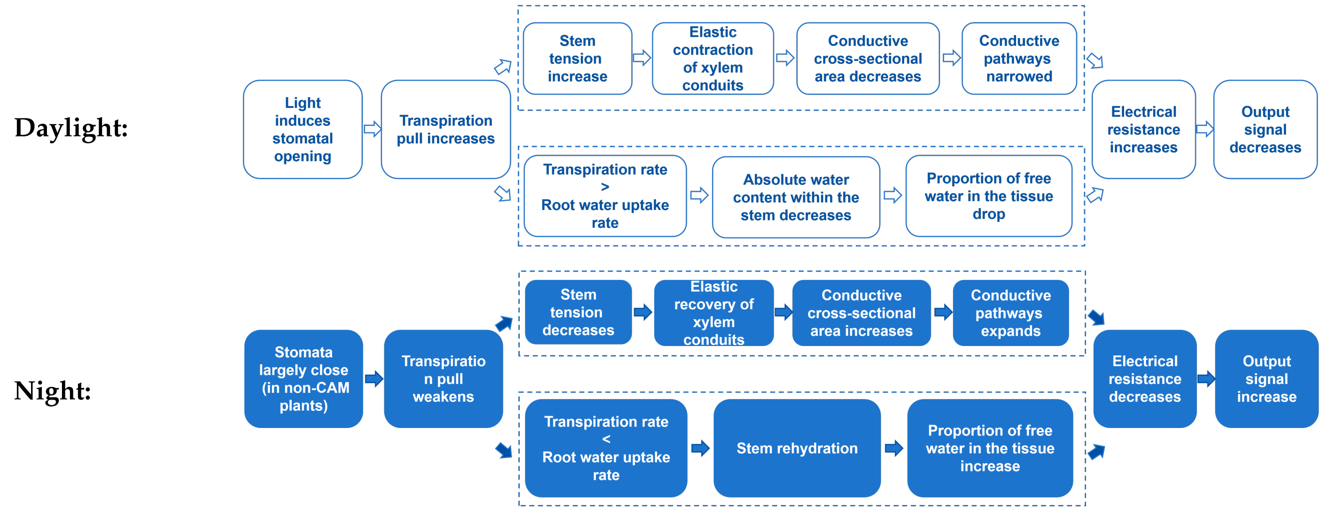

Based on the aforementioned signal fluctuation process, when light exhibits periodic rhythmic changes, the stem hydration level of living plants will also undergo rhythmic variations, allowing the P-C^{4}D sensors to capture these rhythmic signals. Conversely, because the water status of dead plants remains nearly constant, the P-C^{4}D sensors cannot acquire effective signal fluctuations. However, due to individual differences among plants, such as variations in bark thickness, xylem vessel size, and ion concentration, the equivalent resistance and capacitance of the plant tissues vary significantly. Consequently, their electrical impedance fluctuations and the corresponding signals acquired by the sensors differ even under identical physiological states. Therefore, an indicator that mitigates individual differences must be introduced to address 'Challenge 2'. In this study, a rhythm correlation factor is introduced, calculated as follows:

(1) Acquire the output signal sequence of the tested sample over a 24 h period, denoted as $U_{out}(t)$, and define a standard fluctuation signal sequence $U_{st}(t)$ (as shown in Figure 7) of the same length.

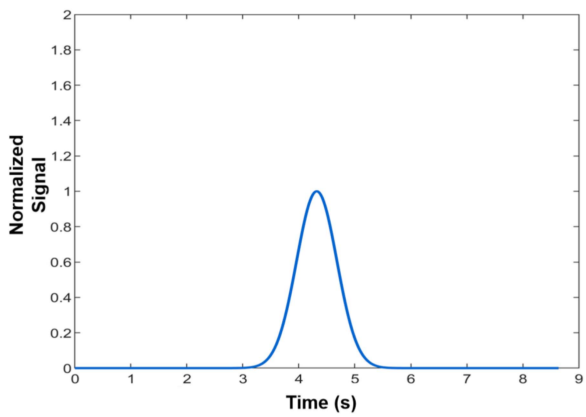

Figure 7. Standard fluctuation signal sequence.

(2) Normalize $U_{out}(t)$ to the range $[-1, 1]$ using Equation (1) to obtain $U_o(t)$,

$$U_o(t) = \left(\frac{U_o(t) - \min(U_o(t))}{\max(U_o(t)) - \min(U_o(t))} - 0.5\right) \times 2 \tag{1}$$

(3) Calculate the cross-correlation function $\mathrm{Corr(i)}$ between $\mathrm{U_o(t)}$ and $\mathrm{U_{st}(t)}$ according to Equation (2), denoted as:

$$\mathrm{Corr(i)} = \frac{1}{\mathrm{T}}\sum_{\mathrm{t=1}}^{\mathrm{T}} \mathrm{U_o(t)U_{st}[(t+i)]} \tag{2}$$

(4) Search for the peak value of the cross-correlation function $\mathrm{Corr(i)}$, which is designated as the rhythm correlation coefficient $\mathrm{CR_{p-s}}$:

$$\mathrm{CR_{p-s}} = \max(\mathrm{Corr(i)}) \tag{3}$$

(5) If $\mathrm{CR_{p-s}} > \varepsilon_{\mathrm{p-s}}$ ($\varepsilon_{\mathrm{p-s}}$ is set to 25,000 in this study), it indicates that the single-day signal fluctuations of the corresponding plant sample are significantly correlated with the standard fluctuations, demonstrating a distinct rhythm; thus, the sample is identified as viable. Conversely, if the threshold is not met, it indicates the absence of a distinct rhythm, and the sample is defined as inactive.

2.4.3. Stress Quantification

After surviving samples are identified through rhythm correlation analysis, the Fuzzy C-Means (FCM) algorithm is employed to further distinguish water stress. Considering that water stress is a gradual process with quantifiable degrees, this presents a typical soft classification problem. As a classic soft clustering algorithm, FCM is well-suited for this task [51,52]. The procedure is as follows:

i. Conduct preliminary experiments to establish a sample library and record the extracted feature vectors. The nth feature vector, denoted as η_n, consists of the peak-to-peak value of $\mathrm{U_{out}(t)}$ (the difference between the maximum and minimum values, $\mathrm{U_{p-p}}$), the average slope of the rising segment ($\mathrm{l_{up}}$), and the average slope of the falling segment ($\mathrm{l_{down}}$) derived from the plant fluctuation signal Uoutt. Thus, it can be expressed as $\eta_n = \begin{bmatrix} \mathrm{U_{p-p}} & \mathrm{l_{up}} & \mathrm{l_{down}} \end{bmatrix}$.

ii. Solve the following optimization problem:

$$\begin{aligned} &\min\left(\sum_{n=1}^{N} s_{\mathrm{Normal},n}{}^{m}\|\eta_n - c_b\|^2 + \sum_{n=1}^{N} s_{\mathrm{Stress},n}{}^{m}\|\eta_n - c_s\|^2\right) \\ &\text{s.t.} \quad s_{\mathrm{Normal},n} + s_{\mathrm{Stress},n} = 1\ (n = 1, 2, \ldots, N) \end{aligned} \tag{4}$$

where c_{Normal} and c_{Stress} represent the cluster centers corresponding to the two extreme states of "normal watering" and "extreme water stress," respectively; $s_{\mathrm{Normal},n}$ denotes the membership degree of the nth feature vector to "normal watering," while $s_{\mathrm{Stress},n}$ denotes its membership degree to "extreme water stress"; m represents the fuzzy coefficient; $\|\eta_n - c_{\mathrm{Normal}}\|^2$ and $\|\eta_n - c_{\mathrm{Stress}}\|^2$ indicate the Euclidean distances from the feature vector to the two cluster centers.

The solution involves the following steps:

Step 1: Initialize the membership degrees to 0.5 for both states, i.e., $s^0_{\mathrm{Normal},n} = s^0_{\mathrm{Stress},n} = 0.5(n = 1, 2, \ldots, N)$. Set the fuzzy coefficient m = 2 based on empirical selection, set the iteration counter i to 0, and define the iteration termination threshold $\varepsilon_{\mathrm{FCM}} = 10^{-5}$.

Step 2: Using the membership degrees from the previous iteration $s^i_{b,n}$ and $s^i_{s,n}$ (the ith iteration), calculate the cluster centers for the current iteration cycle c_b^{i+1} and c_s^{i+1} (the i+1th iteration) according to Equations (5) and (6).

$$c^{i+1}_{\mathrm{Normal}} = \frac{\sum_{n=1}^{N}\left(s^i_{\mathrm{Normal},n}{}^{m}\right)\eta_n}{\sum_{n=1}^{N} s^i_{\mathrm{Normal},n}{}^{m}} \tag{5}$$

$$c_{\mathrm{Stress}}^{i+1}=\frac{\sum_{n=1}^{N}\left(s_{\mathrm{Stress},n}^{i}{}^{m}\right)\eta_n}{\sum_{n=1}^{N}s_{\mathrm{Stress},n}^{i}{}^{m}} \tag{6}$$

Step 3: Using the newly updated cluster centers c_b^{i+1} and c_s^{i+1}, recalculate the membership degrees for the current iteration $s_{\mathrm{Normal},n}^{i+1}$ and $s_{\mathrm{Stress},n}^{i+1}$.

$$s_{\mathrm{Normal},n}^{i+1}=\left[\left(\frac{\left\|\eta_n-c_{\mathrm{Normal}}^{i+1}\right\|^2}{\left\|\eta_n-c_{\mathrm{Stress}}^{i+1}\right\|^2}\right)^{\frac{1}{m-1}}+1\right]^{-1} \tag{7}$$

$$s_{\mathrm{Stress},n}^{i+1}=\left[\left(\frac{\left\|\eta_n-c_{\mathrm{Stress}}^{i+1}\right\|^2}{\left\|\eta_n-c_{\mathrm{Normal}}^{i+1}\right\|^2}\right)^{\frac{1}{m-1}}+1\right]^{-1} \tag{8}$$

Step 4: Calculate the variation Δs between the membership results of the current and previous iterations.

$$\Delta s=\sum_{n=1}^{N}\left[\left(s_{\mathrm{Normal},n}^{i+1}-s_{\mathrm{Normal},n}^{i}\right)^2+\left(s_{\mathrm{Stress},n}^{i+1}-s_{\mathrm{Stress},n}^{i}\right)^2\right] \tag{9}$$

If $\Delta s < \varepsilon_{\mathrm{FCM}}$, terminate the iteration and output the final membership degrees $s_{\mathrm{Normal},n}^{i+1}$ and $s_{\mathrm{Stress},n}^{i+1}$ and cluster centers $c_{\mathrm{Normal}}^{i+1}$ and $c_{\mathrm{Stress}}^{i+1}$. Otherwise, increment the iteration counter i by 1 and return to Step 2.

iii. Actual stress quantification: Utilize the corresponding P-C^4D sensor to obtain the output signals from the tested plant samples and extract the relevant feature vector η. Apply the established formulas to separately calculate the membership degrees of the extracted feature vector η to the "normal watering" center (c_{Normal}) and the "water stress" center (c_{Stress}), i.e., s_{Normal} and s_{Stress}:

$$s_{\mathrm{Normal}}=\left[\left(\frac{\|\eta-c_{\mathrm{Normal}}\|}{\|\eta-c_{\mathrm{Stress}}\|}\right)^{\frac{1}{m-1}}+1\right]^{-1} \tag{10}$$

$$s_{\mathrm{Stress}}=1-s_{\mathrm{Normal}} \tag{11}$$

iv. Use the membership degree to the "water stress" center (s_{Stress}) as the quantitative indicator for plant water stress. If $s_{\mathrm{Stress}} \leq 0.3$, the plant is considered to be in a relatively normal watering state. If $0.3 < s_{\mathrm{Stress}} \leq 0.7$, the plant is experiencing water stress and requires increased irrigation. If $s_{\mathrm{Stress}} > 0.7$, the plant is under severe water stress and necessitates manual intervention. It is important to note that these thresholds are specific to the statistical distribution of the current dataset and serve as preliminary indicators. They should not be considered universal biological constants and warrant further validation against physiological reference standards in future studies.

The two sets of experiments (24 experiments per set) were respectively used to prepare the FCM training set and the test set for algorithm validation. The 24 experiments designated for the training set were expanded to 120 through data augmentation (random weighted averaging of similar signals) and employed to establish the FCM model (steps i and ii), while the remaining 24 experiments were processed via steps iii and iv to obtain stress quantification results ().

3. Experimental Results

3.1. Sensor Performance Simulation

First, simulations were conducted to demonstrate that the proposed offset semi-annular electrodes can maintain effective contact throughout plant physiological behaviors (water absorption, water loss, and other kind of water-related swelling/shrinkage) that cause diameter changes, while exhibiting measurement sensitivity comparable to that of traditional ring-shaped electrodes. The simulation results are presented in Figure 8.

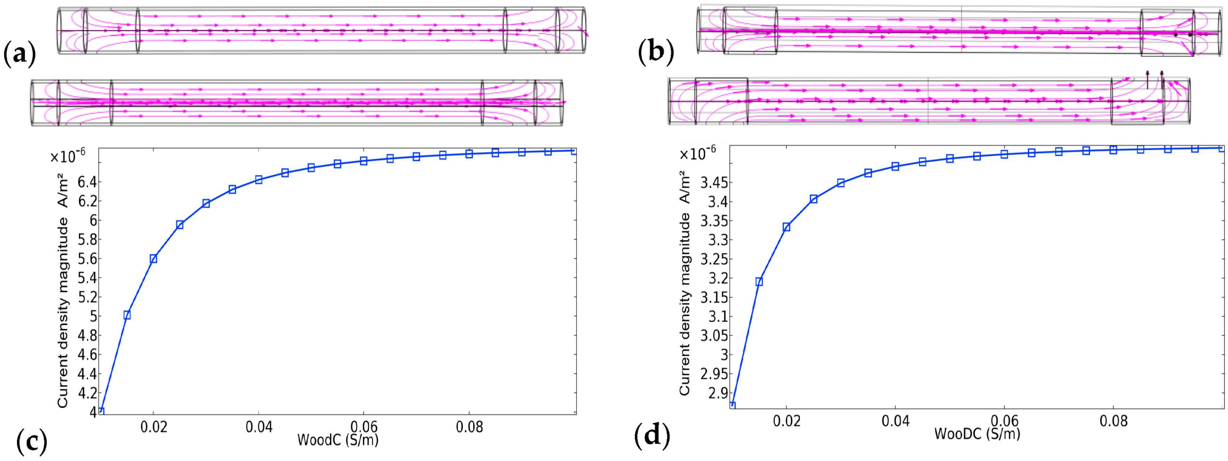

Figure 8. Simulation results of Sensor Performance: (**a**) Current density distribution of traditional ring-shaped electrodes, (**b**) Current density distribution of semi-annular electrodes, (**c**) Output vs. conductivity of traditional ring-shaped electrodes, (**d**) Output vs. conductivity of semi-annular electrodes. The *y*-axis of (**c**,**d**) represents the current density magnitude (A/m^2), which is inversely proportional to the equivalent electrical resistance of the plant tissue. Higher values indicate lower resistance and higher tissue water content. The arrows indicate current direction in Figure 8a,b.

Figure 8a,b illustrate the current density distributions for the designed semi-annular electrodes and the classic ring-shaped electrodes, respectively. It is evident that in both configurations, the current effectively passes through the central region of the target object. Figure 8c,d compare the signal outputs of the two electrode configurations under identical conditions as the electrical conductivity of the internal medium within the tested pipe varies (simulating the process of moisture fluctuation). Although the current amplitudes differ between the two—primarily due to differences in coupling capacitance—their similar magnitudes indicate that both configurations exhibit comparable sensitivity to variations in water status.

3.2. Correlation Between Electrical Signals and Water Loss of Detached Stems

To examine the correlation between electrical signals and water loss during dehydration, a 48 h gravimetric natural dehydration assay was conducted using detached stem samples. The weight loss of the samples was monitored via a high-precision balance, while the electrical signals were simultaneously recorded by the proposed sensor. A natural dehydration process was selected over artificial drying to preserve tissue viability and prevent rapid cell necrosis, which could alter ionic conduction pathways. The absolute water content (W) was determined gravimetrically based on the weight loss relative to the dry mass, calculated as follows:

$$W = \frac{M_t - M_{dry}}{M_{dry}} \times 100\%$$

where M_t is the real-time mass of the sample, and M_{dry} is the constant mass obtained after oven-drying the sample at the conclusion of the experiment.

The temporal evolution of the absolute water content and the corresponding sensor output is illustrated in Figure 9a. As indicated by the gravimetric data, a rapid water loss rate was initially observed, which gradually decelerated over time. A consistent downward trend in the sensor output (corresponding to an increase in electrical resistance) was exhibited as dehydration progressed. However, it is noted that the rate of change in the electrical signal was relatively uniform and appeared slower than the rapid water loss observed in the initial stage. To further quantify the correlation between electrical signals and water loss in detached stems, the sensor output was plotted against the sample absolute water content in Figure 9b. It should be noted that this assay specifically demonstrates the signal–water loss correlation in excised tissues and does not constitute comprehensive physiological validation for intact plants. A strong positive correlation is confirmed by this plot: as the water content decreases, the electrical signal is shown to decrease monotonically, by which the sensor's capability to track dynamic water changes is validated.

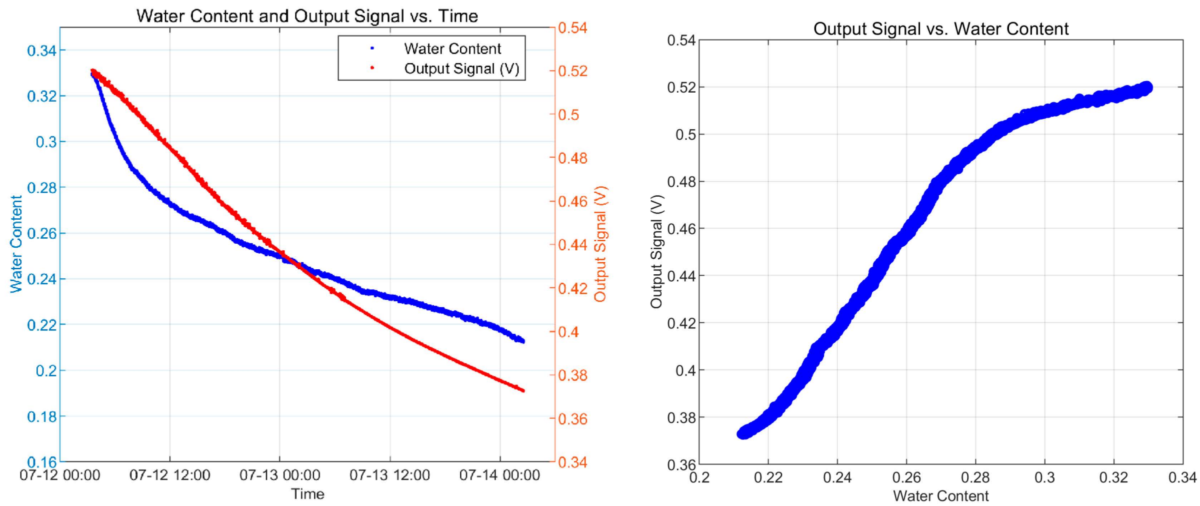

(**a**) (**b**)

Figure 9. (**a**) Temporal evolution of absolute water content and sensor output during natural dehydration. (**b**) Correlation between sensor output and absolute water content.

The discrepancy in the rate of change observed in the initial stage (Figure 9a,b) is attributed to two primary factors related to the measurement mechanism and plant physiology:

1. Capacitive Coupling Effect: The C^4D measurement principle involves a coupling capacitor (C_{epi}) connected in series with the solution resistance (R_{xylem}), as depicted in Figure 1a. In the initial stage of dehydration, the tissue water content is high, resulting in a relatively low R_x. Under these conditions, the impedance of the constant coupling capacitor ($Z_c = 1/j\omega C_{epi}$) is considered to constitute a significant portion of the total impedance. Consequently, the signal magnitude is buffered by this capacitive background, even when R_{xylem} is increased rapidly due to fast water loss.

2. Spatial Heterogeneity of Water Loss: In detached stems, water loss is known to occur heterogeneously. Initially, "free water" is primarily lost from the cut ends and xylem vessels. However, the bound water within the cells and the moisture in the middle section of the stem (where the sensor was mounted) are maintained at a relatively stable level during this early phase. Since the local impedance at the mounting position is detected by the sensor, a conductive pathway is sustained despite the rapid global weight loss at the

cut ends. As a result, the electrical signal is observed to decrease more gradually than the total mass of the sample.

3.3. Effectiveness of Rhythm Correlation Factors CR_{p-s}

Figure 10a–d presents the cross-correlation functions and corresponding CR_{p-s} between Uou and Us under multiple states. These reference signals were generated through simulation experiments to evaluate the validity and rationality of the rhythm factor CR_{p-s}.

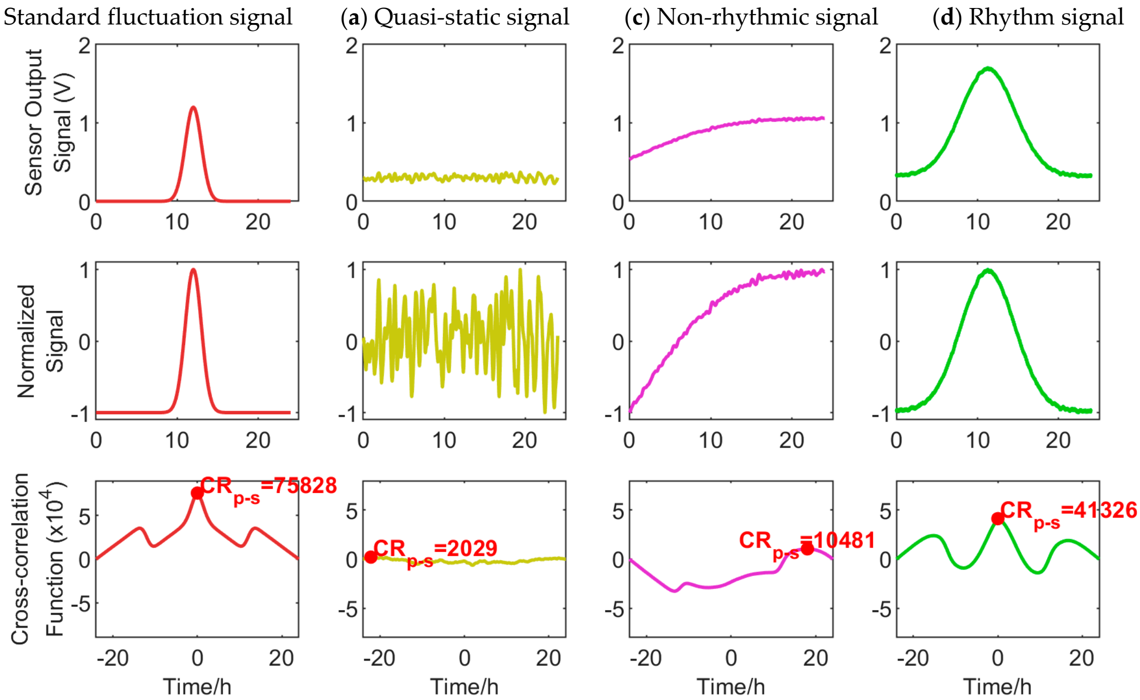

Figure 10. Effectiveness of CR_{p-s}: (**a**) Standard fluctuation signal, (**b**) Quasi-static signal, (**c**) Non-rhythmic signal, (**d**) Rhythm signal.

Figure 10a shows the standard fluctuation signal itself, $CR_{p-s} = 75,828$. Figure 10b represents a quasi-static signal with noise, $CR_{p-s} = 2029$, which indicates the typical manifestation of inactive plants; specifically, the stem water status and output signal remain virtually unchanged. However, after normalization, the noise is significantly amplified. Figure 10c illustrates a non-rhythmic signal, $CR_{p-s} = 10,481$, which occasionally appears in inactive plants. Due to complete physiological failure, the xylem and pith lose their ability to regulate water. Consequently, soil moisture continuously enters through the compromised epidermis, resulting in a monotonic increase in stem hydration level and a continuously rising output signal. Figure 10d depicts a typical rhythm signal, $CR_{p-s} = 41,326$. As shown in Figure 10, active plants exhibit synchronized water fluctuations with light conditions, thereby yielding a rhythmic signal. As illustrated, signals exhibiting rhythmic variations demonstrate significantly higher CR_{p-s} values compared to non-rhythmic signals.

3.4. Physiological State Identification Experiment

Based on the extracted electrical conductivity fluctuation signals, an analysis of the signal characteristics was conducted. Figure 11a is the standard fluctuation signal used in this experiment, Figure 11b is the reference signal obtained in this experiment. In Figure 11c–f, the variation process of equivalent conductivity signals over a 24 h period for these plant samples under typical water physiological states is illustrated; (c) and (d) are viable samples, (e) is a stress sample, and (f) is an inactive sample.

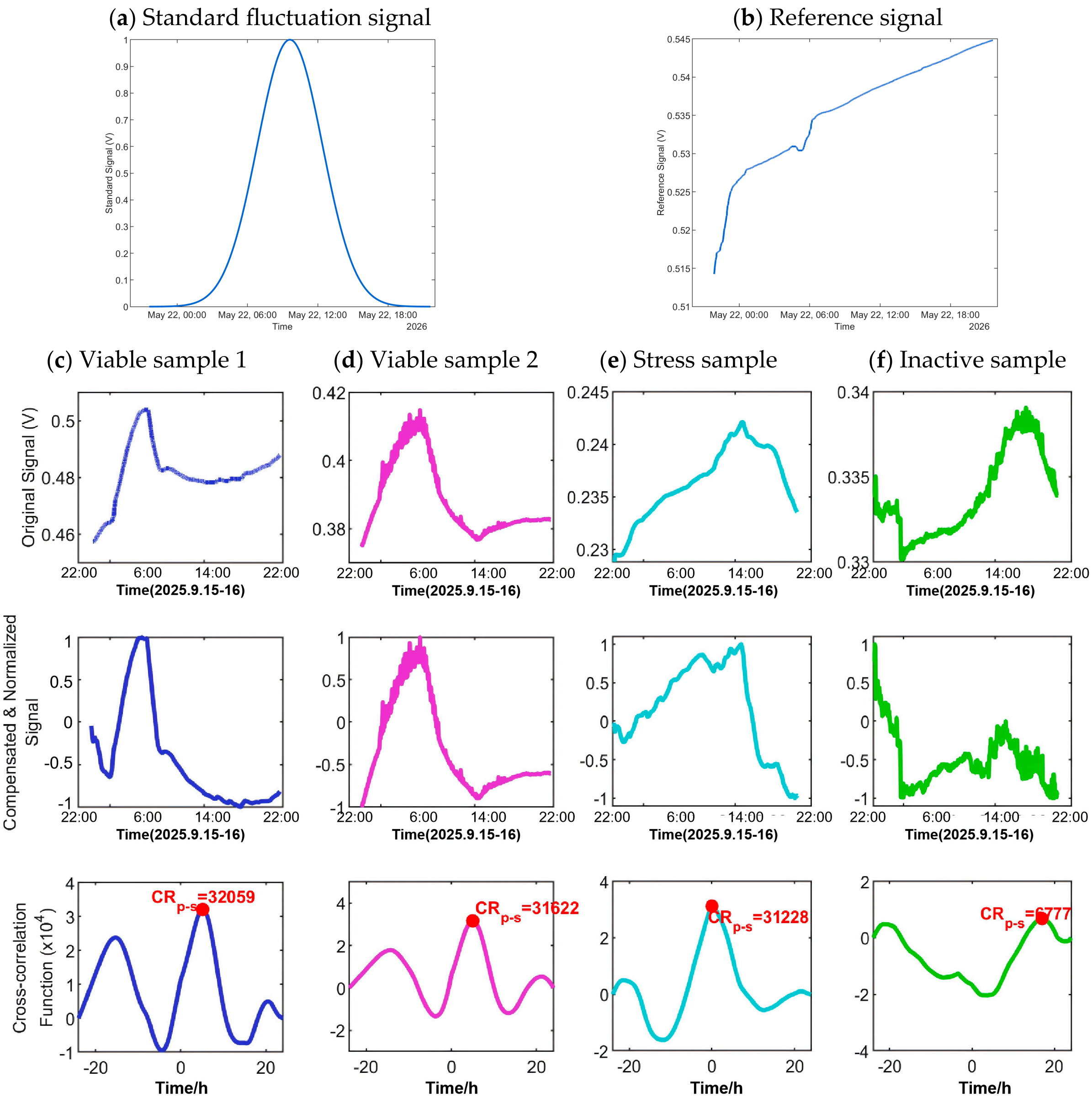

Figure 11. Physiological State Identification Experimental result: (**a**) Standard fluctuation signal, (**b**) Reference signal, (**c**) result of 'Viable sample 1', (**d**) result of 'Viable sample 2', (**e**) result of ' Stress sample', (**f**) result of 'Inactive sample'.

Observations from the figures reveal distinct characteristic differences across the three physiological states:

(1) As shown in Figure 11c,d, when plants are under sufficient water supply, light acts as the dominant factor driving water fluctuations. From 22:00 to 6:00, due to the absence of light, most leaf stomata remain closed, resulting in weak transpiration. During this period, root water absorption gradually replenishes the stem water deficit accumulated from the previous day, causing the sensor output signal to continuously rise. Upon the onset of illumination at 6:00, stomata open and transpiration is initiated. Since the rate of root water absorption is lower than the rate of transpirational water loss, the stem hydration level continues to decline until it reaches the physiological regulation threshold. At this point, the plant actively closes a portion of its stomata to reduce the rate of water loss. Correspondingly, the sensor output signal initially decreases before stabilizing, eventually returning to the pre-absorption levels observed on the previous day. Overall, the P-C^{4}D

sensor output exhibits a pronounced rhythm synchronized with light cycles, aligning with normal plant physiological activity trends.

(2) As shown in Figure 11e, when plants are experiencing water stress, light retains its regulatory capacity over transpiration. However, due to the extremely limited water availability in the soil, although the P-C^4D sensor output still follows certain rhythms correlated with light, both the signal amplitude and fluctuation magnitude are significantly reduced compared to those under sufficient water supply. Experimental observations further indicate a positive correlation between the severity of water stress and the degree of reduction in output signal amplitude and fluctuation magnitude.

(3) As shown in Figure 11f, once plants are completely inactivated, there is no water transport behavior driven by physiological activity, resulting in an almost constant sensor output. Additionally, a very small number of inactivated samples exhibited a continuous increase in signal. This phenomenon is attributed to the disintegration of cellular structures following plant tissue death, which causes residual moisture in the soil and roots to migrate continuously via capillary action.

To further validate the effectiveness of the rhythmic correlation coefficient in determining plant survival status, an independent samples t-test was performed between the two groups. The results demonstrated a highly significant difference ($t = -10.04$, $p < 0.001$). The mean coefficient for Type 2 (Viable sample) was 30,131.84 (95% CI [27,459.06, 32,804.62]), which was significantly higher than that of Type 1 (Inactive sample) (8651.60, 95% CI [6443.35, 10,859.85]). The non-overlapping confidence intervals confirm that this metric can reliably distinguish between different survival states, verifying its discriminative efficacy for survival status but not equating to FCM model evaluation.

3.5. Stress Quantification Experiment

To ensure the robustness of the clustering model, data augmentation technique are employed on the raw signals. The original dataset, consisting of approximately 40 experimental groups (Normal:Mild stress: Severe stress = 7:7:6), was expanded to 120 samples by adding Gaussian noise and applying non-linear weighting to samples with the same status. Subsequently, the Fuzzy C-Means (FCM) algorithm was applied to classify the samples into two distinct states: "normal watering" and "extreme water stress."

The clustering centers were determined based on the feature vectors (Range, Ascending Mean, and Descending Mean). As shown in Table 2, Cluster 1 corresponds to the extreme water stress state (characterized by lower signal amplitude and range), while Cluster 2 represents the normal watering state. To validate the reliability of the model, the FCM classification results were compared with the actual irrigation strategies (Ground Truth). The analysis demonstrated a high consistency between the clustering results and the experimental observations, confirming that the extracted features effectively distinguish between the physiological states of the plants.

Table 2. Feature vectors of the FCM cluster centers.

Cluster	State Description	Range	Ascend Mean	Descend Mean
Cluster 1	extreme water stress	0.01034	5.191×10^{-7}	8.731×10^{-8}
Cluster 2	normal watering	0.07156	2.682×10^{-6}	8.926×10^{-7}

The table (Table 3) below presents the experimental results for the identification of water physiological states.

Table 3. Water physiological states identification and stress quantification result.

No.	State	Predicted Viability	s_{Stress}	No.	State	Predicted Viability	s_{Stress}
1	N (Normal)	√	0.11	13	MS	√	0.42
2	N	√	0.19	14	MS	√	0.62
3	N	√	0.03	15	SS (Severe stress)	√	0.57
4	N	√	0.21	16	SS	√	0.77
5	N	√	0.24	17	SS	×	/
6	N	√	0.12	18	SS	√	0.87
7	N	√	0.24	19	SS	√	0.74
8	MS (Mild stress)	√	0.42	20	SS	×	/
9	MS	√	0.39	21	I (Inactive)	×	/
10	MS	√	0.45	22	I	×	/
11	MS	√	0.67	23	I	×	/
12	MS	√	0.55	24	I	×	/

As shown in Table 3, experimental results on 24 samples show a discrimination accuracy (the proportion of test samples correctly classified among all original test samples) of 91.67% (22/24 correct). The experimental results presented above demonstrate that the overall identification performance is satisfactory, and that the FCM algorithm can effectively quantify the degree of stress. However, it should be noted that a very small number of samples under severe water stress were incorrectly identified as inactivated. This misclassification occurs because plants subjected to extreme water deficit may activate protective mechanisms, closing their stomata and halting transpiration even under illumination. Consequently, no effective rhythmic signals can be detected. In practical applications, this physiological transition typically develops gradually. Therefore, the proposed method allows for the early detection of such issues, enabling timely intervention.

3.6. Discussion

3.6.1. Primary Mechanisms of Individual Differences Affecting Measurements

As previously discussed, the influence of individual differences is unavoidable. In this study, comparative experiments and simulation analyses were conducted concurrently to identify the primary mechanisms by which individual differences affect measurements. Based on the measurement mechanism illustrated in Figure 1a, the main sources of individual differences are identified as morphological parameters—specifically bark thickness, xylem thickness, pith diameter, and surface roughness. Unlike water status, these static structural factors alter the effective cross-sectional area of the sensing field, thus influencing the baseline electrical response independent of the plant's hydration level.

(1) Influence of the Bark: The bark serves as the primary medium generating coupling capacitance; therefore, its properties are directly correlated with the coupling capacitance. Coupling capacitance acts as a background factor in xylem moisture content measurements. In industrial applications, increasing the excitation frequency is commonly employed to mitigate the impact of coupling capacitance [44–46]. However, in practical scenarios, excessively high excitation frequencies exacerbate the interference from stray capacitance between wires, which is detrimental to actual measurements. Consequently, it is essential to clarify the specific effects of the bark to guide subsequent sensor optimization. As bark thickness increases, the coupling capacitance decreases, thereby exerting a greater influence on the measurement. Conversely, higher water content in the bark leads to a larger dielectric constant and reduced coupling capacitance, diminishing its impact. Nevertheless, excessive water content causes the bark to exhibit significant resistive characteristics, altering the sensor's measurement pathway. This may result in the measurement current flowing directly through the bark, thereby attenuating the effective measurement signal. Furthermore, bark roughness affects the volume of adhesive filling the gap between the

electrodes and the bark, subsequently influencing the coupling capacitance. Roughness also impacts the mechanical stability of electrode installation.

(2) Influence of the Xylem: The xylem serves as the primary conduit for water transport, and its hydration dynamics are the core determinant of the stem's equivalent electrical conductance. However, inherent variations in xylem properties can decouple the electrical signal from the absolute water status. Firstly, differences in microscopic anatomical structures—such as vessel density, lumen diameter, and pit connectivity—collectively determine the effective cross-sectional area for ion transport. Consequently, even under identical macroscopic water content, plants with distinct anatomical traits may exhibit different baseline equivalent resistances. This highlights that impedance measures the continuity of the conductive pathway rather than a simple volumetric water content. Secondly, the ion concentration of the xylem sap varies due to metabolic regulation, constituting a source of background noise independent of water volume. Crucially, these electrical variations reflect changes in tissue hydration and conductivity, which serve as a proxy for water transport dynamics rather than a direct measure of physiological stress (e.g., pressure potential). Therefore, while these factors complicate cross-plant comparability, the sensor effectively captures relative diurnal fluctuations. In addition to the normalized cross-correlation algorithm employed in this study, introducing impedance spectroscopy to decouple these anatomical and chemical factors will be a critical direction for future research.

(3) Influence of the pith: Compared to the xylem moisture content, which exhibits a pronounced periodic rhythm, the pith moisture content remains relatively stable; however, inherent variations in baseline pith moisture among individual plants still affect the equivalent electrical impedance of the stem, constituting one of the key factors contributing to inter-plant differences in impedance characteristics. The results demonstrate that altering only the pith moisture content induces an overall baseline shift in the impedance signal without altering its dynamic trend correlated with xylem moisture variation. To mitigate this baseline interference caused by inter-plant pith variability, the proposed algorithm—combining signal normalization with cross-correlation against a reference signal—is employed: normalization effectively removes amplitude and baseline deviations induced by pith moisture differences, while cross-correlation further extracts and preserves waveform features highly consistent with xylem water dynamics, thereby significantly enhancing the comparability and analytical accuracy of impedance signals across different plants.

(4) In addition, the phloem and cambium may also exert some influence. However, due to their significantly smaller thickness compared to the xylem region, their effects are obscured by noise owing to the limited sensitivity of the sensor, making them impossible to evaluate at present. Optimization of the sensor's signal-to-noise ratio (SNR) and sensitivity is expected to facilitate real-time detection of these tissues.

3.6.2. Selection of the Time Window

During the experiments, it was found that the selection of the time window for the state identification process significantly affects the measurement, specifically regarding the window length and its start and end points.

Since the identification is based on the cross-correlation function between the data within the window and the standard data, its essence lies in comparing the similarity in shape between the acquired signal and the standard signal. Therefore, the selected time window must encompass a complete rhythm signal of stem water status fluctuation (i.e., one complete cycle of stem hydration level rise and fall). A window that is too narrow may fail to capture valid fluctuations, while an excessively long window might capture multiple fluctuation cycles; both scenarios can lead to deviations in the calculated $CRp-s$, thereby causing misjudgments. In this study, a 24 h time window was selected, which can effectively capture the fluctuation rhythm signals. Furthermore, the choice of the window's start and end points affects the overall shape of the curve. To address this, comparative experiments with different window start times were specifically conducted (Figure 12). The results indicate that when plants are in a normal growth state, the optimal strategy is to position the peak of light intensity at the center of the time window.

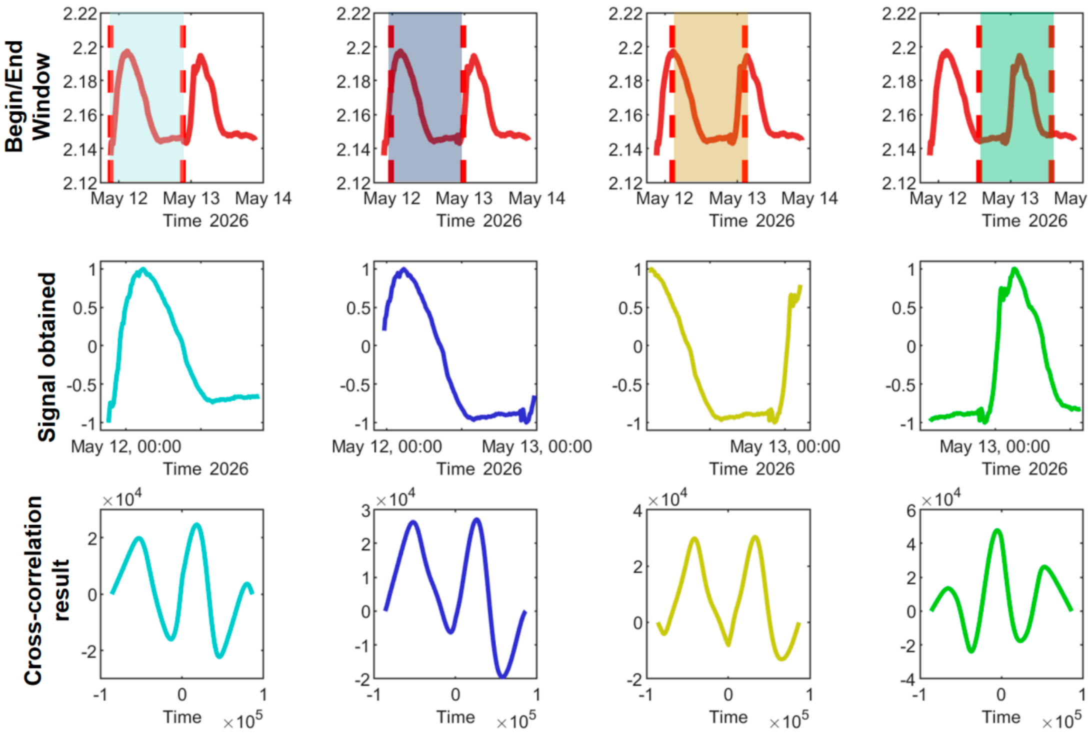

Figure 12. Comparative result of different window start times.

3.6.3. Comparison with Existing Technologies and Field Prospects

To better position the proposed method within the landscape of plant physiological monitoring, it is essential to compare it with existing advanced technologies. While several techniques have been developed to overcome the limitations of traditional methods, each presents distinct constraints in field applications. Electrical Impedance Spectroscopy (EIS) provides a non-destructive alternative by evaluating plant water status through frequency-dependent current flow [24,27–29]; however, its accuracy is highly sensitive to electrode–plant contact conformity and environmental interference, making long-term in situ monitoring challenging [24]. Micro-tensiometers directly measure stem water tension with high precision [53,54], but they suffer from frequent cavitation-induced failures and require complex maintenance in field conditions [55,56]. Sap flow sensors, while effective for estimating transpiration rates, rely on empirical heat dissipation models [57,58] that must be specifically calibrated for different species and stem sizes, limiting their universal applicability [54,57,58], and its accuracy also be influence by the xylem wood healing during long-term measurement. Flexible/wearable sensors offer conformal contact, but their long-term stability and signal drift under fluctuating outdoor environments remain unresolved (i.e., Challenge 3 mentioned above) [59–61]. To more clearly contrast the strengths and weaknesses of these methods with the proposed approach, a comparison is conducted from the perspectives of measurement invasiveness, temporal resolution, calibration requirements, sensitivity to tissue structure, and potential effects of environmental or anatomical variations; the results are summarized in Table 4.

Table 4. Comparative Analysis of Plant Water Status Monitoring Techniques.

	EIS [24,27–29]	Micro-Tensiometers [53–56]	Sap Flow Sensors [57,58]	Flexible/Wearable Sensors [59–61]	Proposed Method
Measurement invasiveness	Non-invasive	Invasive *1	Invasive	Non-invasive	Non-invasive
Temporal resolution	Real-time	Real-time	Continuous	Real-time	Real-time
Calibration requirements	Species-dependent	Minimal	High (species/size-dependent)	Model-dependent	Low
Sensitivity to tissue structure/ anatomical variations	Medium (xylem conductivity)	Low	Medium (xylem wood healing)	High	Medium (Stem size)
Environmental	High (temperature, humidity)	Low	Medium (stem geometry)	High (material degradation)	Method-specific *2

Note of Table 4: *1: Micro-tensiometers require physical insertion into plant tissue, but do not disrupt flow. *2: Environmental noise is compensated (Section 2.4.1).

In contrast, the proposed sensor demonstrates improved robustness and stability under controlled laboratory conditions for continuous plant water status monitoring, though its performance in field environments remains unverified. Specifically, while it mitigates contact-dependent issues (e.g., electrode conformity in EIS) and maintenance challenges (e.g., cavitation in micro-tensiometers) within the scope of our single-cultivar experimental setup, broader applicability to woody plants requires validation across diverse species, field conditions, and environmental variables.

While this study establishes the fundamental feasibility of the proposed C^4D-based approach, we acknowledge that the validation was limited to a specific cultivar under controlled laboratory conditions. Consequently, the immediate generalizability of the method to complex agricultural scenarios remains to be fully assessed. Moving towards field application requires addressing significant challenges regarding both biological diversity and environmental robustness. In actual agricultural operations, uncontrollable factors—such as fluctuating temperature, light intensity, and soil moisture—can introduce noise that interferes with measurement signals. Furthermore, variations in tissue structure and water transport dynamics across different species necessitate a broader validation scope. Therefore, our future work will prioritize: (1) enhancing system robustness through multi-sensor information fusion to decouple environmental interferences; and (2) conducting extensive validation involving additional biological replicates and diverse woody species. These steps are essential to build a comprehensive feature database and ensure the method's reliability for field-grown plants.

Furthermore, while capacitive effects were partially accounted for in our equivalent amplitude measurements, the resistive and capacitive components of the stem tissue have not yet been completely decoupled. To bridge the gap between relative electrical signals and absolute physiological metrics (such as water potential Ψ measured by conventional psychrometry [20]), a comprehensive multi-physics sensing approach will be explored. Specifically, we aim to evolve the current sensor into a non-invasive Electrical Spectroscopy Imaging (ESI) system. By integrating phenotypic analysis with controlled laboratory experiments, we seek to elucidate the intrinsic correlations between optimized impedance spectral signals and plant physiological traits, thereby achieving precise component decoupling and absolute quantification.

Building upon this accurate assessment of stem water status, our future research will advance along a second strategic direction to further bridge the gap between physiological monitoring and precision agriculture. We will focus on algorithmic optimization to derive dynamic sap flow data. This will enable the continuous quantification of transpiration and real-time water physiological status, ultimately providing actionable, data-driven insights for precision irrigation management.

4. Conclusions

This paper draws upon the principles of non-contact industrial fluid measurement to propose a novel non-invasive method for real-time monitoring of plant water status based on xylem electrical conductivity, By establishing the correlation between electrical impedance and hydraulic continuity, this method overcomes the limitations of invasive techniques, enabling online, in situ, and non-invasive monitoring of water stress in woody plant stems. The main work and findings are summarized as follows:

(1) The industrial C4D sensing system is adaptively modified to construct a specialized pC4D sensor for stem monitoring, and an array-based measurement system is designed for batch signal acquisition from multiple plant samples.

(2) Full-day dynamic experiments are conducted under three states: normal water supply, varying degrees of water stress, and plant inactivation. Sensitive characteristic parameters representing water physiological status are extracted through signal analysis, effectively capturing the dynamic variations in stem water content and the disruption of the hydraulic pathway induced by water deficit.

(3) Drawing on industrial multiphase flow pattern identification theory, a pattern recognition-based method for water stress identification is established. Through signal processing techniques including environmental interference elimination and individual difference suppression, the method achieves accurate discrimination between viable and inactivated plant states.

(4) The Fuzzy C-Means (FCM) clustering algorithm is introduced to quantitatively assess the severity of water stress in viable plants. Experimental results on 24 samples show a discrimination accuracy of 91.67% (22/24 correct), and the FCM clustering results are consistent with actual water supply conditions.

It should be noted that all experiments in this study were conducted under controlled laboratory conditions, and the results primarily demonstrate the feasibility and correlation of the proposed method in a simplified environment. Further validation under natural field conditions with intact plants subjected to complex environmental factors remains to be investigated. As a ground-based complement to remote sensing, this method offers a new pathway for continuous, in situ monitoring of plant water status at the stem level, providing a robust tool for studying plant hydraulic safety margins and drought response mechanisms.

Author Contributions: Conceptualization, J.H. (Junchao Huang); methodology, J.H. (Junchao Huang); software, J.H. (Jiahui Huang); validation, J.G., J.H. (Jiahui Huang) and X.Y.; formal analysis, J.H. (Jiahui Huang); investigation, J.H. (Junchao Huang) and J.G.; resources, J.H. (Junchao Huang); data curation, J.G.; writing—original draft preparation, X.Y.; writing—review and editing, J.H. (Junchao Huang); visualization, X.Y.; supervision, J.H. (Junchao Huang); project administration, J.H. (Junchao Huang); funding acquisition, J.H. (Junchao Huang). All authors have read and agreed to the published version of the manuscript.

Funding: This research was funded by " Zhejiang Provincial Natural Science Foundation of China under Grant No. LQ24F030002." and "Research Development Fund of Zhejiang A&F University (No. 2023LFR036)".

Data Availability Statement: The raw data supporting the findings of this study are openly available in GitHub at https://github.com/GreenDog-Huang/Raw-Data-for-2026-Agronomy-HJC.

Acknowledgments: During the preparation of this manuscript, the authors used 'Nano Banana 2.0' for the purposes of generating plants and background elements in Figure 6. The authors have reviewed and edited the output and take full responsibility for the content of this publication.

Conflicts of Interest: The authors declare no conflicts of interest.

References

1. Lambers, H.; Chapin, F.S., III; Pons, T.L. Plant Water Relations. In *Plant Physiological Ecology*, 3rd ed.; Springer: Cham, Switzerland, 2019.
2. Taiz, L.; Zeiger, E. *Plant Physiology*, 4th ed.; Sinauer Associates: Sunderland, MA, USA, 2006.
3. Muturi, J.W.; Ndehedehe, C.E.; Kennard, M.J. A review of the use of remote sensing techniques in assessing irrigation water use. *Agric. Water Manag.* **2025**, *319*, 109759. [CrossRef]
4. Kadyampakeni, D.M.; Scudiero, E.; Shrestha, R. Advances in precision irrigation management in the twenty-first century. *Irrig. Sci.* **2025**, *43*, 989–994. [CrossRef]
5. Chastain, D.R.; Snider, J.L.; Collins, G.D.; Perry, C.D.; Whitaker, J.; Byrd, S.A.; Oosterhuis, D.M.; Porter, W.M. Irrigation scheduling using predawn leaf water potential improves water productivity in drip-irrigated cotton. *Crop Sci.* **2016**, *56*, 3185–3195. [CrossRef]
6. Ye, Y.; Cruz, M.F.G.; Lázaro, R.J.S.; Zamora-Izquierdo, M.A.; González-Vidal, A.; Tortosa, P.N.; Rubio-Asensio, J.S.; Gallud, M.F.O.; Skarmeta, A.F. Optimizing irrigation in peach trees by predicting trunk water potential using machine learning based on FloraPulse microtensiometers. *J. Syst. Archit.* **2026**, *176*, 103814. [CrossRef]
7. Brodersen, C.R.; Roddy, A.B.; Wason, J.W.; McElrone, A.J. Functional Status of Xylem Through Time. *Annu. Rev. Plant Biol.* **2019**, *70*, 407–433. [CrossRef] [PubMed]
8. Slupianek, A.; Dolzblasz, A.; Sokolowska, K. Xylem Parenchyma-Role and Relevance in Wood Functioning in Trees. *Plants* **2021**, *10*, 1247. [CrossRef] [PubMed]
9. Tian, H.; Zhao, Y.D.; Gao, C.; Xie, T.; Zheng, T.; Yu, C.C. Assessing the Vitality Status of Plants: Using the Correlation between Stem Water Content and External Environmental Stress. *Forests* **2022**, *13*, 1198. [CrossRef]
10. Fishman, N.; Yungstein, Y.; Yaakobi, A.; Obersteiner, S.; Rez, L.; Mulero, G.; Michael, Y.; Klein, T.; Helman, D. Leaf Water Potential in a Mixed Mediterranean Forest from Machine Learning and Unmanned Aerial Vehicle (UAV)-Based Hyperspectral Imaging. *Remote Sens.* **2025**, *17*, 106. [CrossRef]
11. Laroche-Pinel, E.; Vasquez, K.R.; Brillante, L. Assessing Grapevine Water Status in a Variably Irrigated Vineyard with NIR/SWIR Hyperspectral Imaging from UAV. *Precis. Agric.* **2024**, *25*, 2356–2374. [CrossRef]
12. Delogu, E.; Boulet, G.; Olioso, A.; Garrigues, S.; Brut, A.; Tallec, T.; Demarty, J.; Soudani, K.; Lagouarde, J.-P. Evaluation of the SPARSE Dual-Source Model for Predicting Water Stress and Evapotranspiration from Thermal Infrared Data over Multiple Crops and Climates. *Remote Sens.* **2018**, *10*, 1806. [CrossRef]
13. Chen, H.; Chen, H.X.; Zhang, S.; Chen, S.X.; Cen, F.L.; Zhao, Q.Z.; Huang, X.Y.; He, T.B.; Gao, Z.R. Comparison of CWSI and Ts-Ta-VIs in Moisture Monitoring of Dryland Crops (Sorghum and Maize) Based on UAV Remote Sensing. *J. Integr. Agric.* **2024**, *23*, 2458–2475. [CrossRef]
14. Li, Y.Y.; Qu, T.T.; Wang, Y.Z.; Zhao, Q.X.; Jia, S.J.; Yin, Z.; Guo, Z.D.; Wang, G.F.; Li, F.Z.; Zhang, W.P. UAV-Based Remote Sensing to Evaluate Daily Water Demand Characteristics of Maize: A Case Study from Yuci Lifang Organic Dry Farming Experimental Base in Jinzhong City, China. *Agronomy* **2024**, *14*, 729. [CrossRef]
15. Liu, J.L.; Jin, J.; Huang, J.; Wu, M.J.; Hao, S.Z.; Jia, H.Y.; Qin, T.D.; Huang, Y.Q.; Chen, D.; Pumijumnong, N. Integrating Data from Unmanned Aerial Vehicles and Sentinel-2 with PROSAIL-5D-Driven Machine Learning for Fuel Moisture Content Estimation in Agroecosystems. *Ecol. Inform.* **2025**, *91*, 103389. [CrossRef]
16. Xu, H.Y.; Sun, H.; Xu, Z.H.; Wang, Y.J.; Zhang, T.; Wu, D.; Gao, J.H. kNDMI: A Kernel Normalized Difference Moisture Index for Remote Sensing of Soil and Vegetation Moisture. *Remote Sens. Environ.* **2025**, *319*, 114621. [CrossRef]
17. Zhang, Y.; Cai, M.Y.; Xiao, X.M.; Yang, X.; Migliavacca, M.; Basara, J.; Zhou, S.; Deng, Y.Z.Z. Immediate and Lagged Vegetation Responses to Dry Spells Revealed by Continuous Solar-Induced Chlorophyll Fluorescence Observations in a Tall-Grass Prairie. *Remote Sens. Environ.* **2024**, *305*, 114080. [CrossRef]
18. Li, M.Q.; Wang, P.X.; Tansey, K.; Sun, Y.F.; Guo, F.W.; Zhou, J. Improved Field-Scale Drought Monitoring Using MODIS and Sentinel-2 Data for Vegetation Temperature Condition Index Generation through a Fusion Framework. *Comput. Electron. Agric.* **2025**, *234*, 110256. [CrossRef]
19. Hassanpour, R.; Majnooni-Heris, A.; Fard, A.F.; Tasumi, M. Spatio-Temporal Monitoring of Plant Water Status Using Optical Remote Sensing Data and In Situ Measurements. *Adv. Space Res.* **2024**, *74*, 4688–4704. [CrossRef]
20. Chen, J.; Chen, C. Uncertainty Analysis in Humidity Measurements by the Psychrometer Method. *Sensors* **2017**, *17*, 368. [CrossRef] [PubMed]
21. Servín, M.A.G.; Chávez, A.K.R.; Sánchez, M.M.; García, J.A.A.; González, R.G.G.; Medina, L.M.C. Needle/Electrode Insertion Device for Measuring Plant Electrical Signals. *J. Plant Res.* **2025**, *138*, 525–531. [CrossRef] [PubMed]

22. Restrepo-Acevedo, A.M.; Guo, J.; Novick, K.; Humphrey, V.; Zweifel, R.; Konings, A.G.; Koch, G.; Knowles, J.; Anderegg, L.D.L.; Peters, J.M.R. Continuous Monitoring of Plant Water Potential: Sensor-Based Approaches and Best Practices. *New Phytol.* **2026**, *251*, 569–588. [CrossRef] [PubMed]
23. Sun, J.; Tan, X.Y.; Li, X.X.; Chen, J.F.; Cai, S.H.; Fan, Y.J.; Xia, R.T.; Shao, B.B.; Sun, S.C. A Review of On-Site Detection Methods for Plant Health Based on Electrical Characteristics. *J. Sens.* **2026**, *2026*, 7479434. [CrossRef]
24. Van Haeverbeke, M.; De Baets, B.; Stock, M. Plant Impedance Spectroscopy: A Review of Modeling Approaches and Applications. *Front. Plant Sci.* **2023**, *14*, 1187573. [CrossRef] [PubMed]
25. Chowdhury, R.I.; Basak, R.; Wahid, K.A.; Nugent, K.; Baulch, H. A Rapid Approach to Measure Extracted Chlorophyll-a from Lettuce Leaves Using Electrical Impedance Spectroscopy. *Water Air Soil Pollut.* **2021**, *232*, 73. [CrossRef]
26. Filippov, R.A.; Solovchenko, A.; Yanykin, D.V. Application of the Impedance Measurement Method to Evaluate the Results of Winter Grafting of Pear Cuttings Using Cold Plasma. *Appl. Sci.* **2023**, *13*, 583.
27. Zhang, B.H.; Dong, Z.W.; Sui, X.N.; Gao, J.L.; Feng, L.L. Detection of Water Content in Tomato Stems by Electrical Impedance Spectroscopy: Preliminary Study. *Comput. Electron. Agric.* **2024**, *219*, 108755. [CrossRef]
28. Chin-Hashim, N.F.; Khaled, A.Y.; Jamaludin, D.; Abd Aziz, S. Electrical Impedance Spectroscopy for Moisture and Oil Content Prediction in Oil Palm (*Elaeis guineensis* Jacq.) Fruitlets. *Plants* **2022**, *11*, 3373. [CrossRef] [PubMed]
29. Serrano-Finetti, E.; Castillo, E.; Hilario, L.M.L. Toward Noninvasive Monitoring of Plant Leaf Water Content by Electrical Impedance Spectroscopy. *Comput. Electron. Agric.* **2023**, *210*, 107907. [CrossRef]
30. Liao, A.M.; Zhou, Q.Y.; Zhang, Y. Application of 3D Electrical Capacitance Tomography in Probing Anomalous Blocks in Water. *J. Appl. Geophys.* **2015**, *117*, 91–103. [CrossRef]
31. Michels, V.; Weigand, M.; Lärm, L.; Muller, O.; Kemna, A. Non-Invasive Phenotyping of Sugar Beet and Maize Roots Using Field-Scale Spectral Electrical Impedance Tomography. *Plant Cell Environ.* **2025**, *48*, 7588–7604. [CrossRef] [PubMed]
32. Basak, R.; Wahid, K.A. A Rapid, Low-Cost, and High-Precision Multifrequency Electrical Impedance Tomography Data Acquisition System for Plant Phenotyping. *Remote Sens.* **2022**, *14*, 3214. [CrossRef]
33. Michels, V.; Chou, C.W.; Weigand, M.; Wu, Y.X.; Kemna, A. Quantitative Phenotyping of Crop Roots with Spectral Electrical Impedance Tomography: A Rhizotron Study with Optimized Measurement Design. *Plant Methods* **2024**, *20*, 118. [CrossRef] [PubMed]
34. Qu, C.; Sun, W.; Hu, D.; Yang, C.; Zhao, T.; Wang, X.; He, Z. Semi-Embedded Flexible Multifunctional Sensor for On-Site Continuous Monitoring of Plant Microclimate. *Comput. Electron. Agric.* **2024**, *216*, 108521. [CrossRef]
35. Qu, C.; Cao, L.; Li, M.; Wang, X.; He, Z. Liquid Metal-Based Plant Electronic Tattoos for In-Situ Monitoring of Plant Physiology. *Sci. China Tech. Sci.* **2023**, *66*, 1617–1628. [CrossRef]
36. Wang, X.; Wen, Y.; Li, P.; Li, Y.; Qin, H.; Zhao, J.; Zhai, X.; Yang, W.; Wu, L. Flexible Sensors for Precision Agriculture: A Mini Review. *TrAC Trends Anal. Chem.* **2024**, *180*, 117946. [CrossRef]
37. Kim, J.Y.; Shin, S.K.; Lee, Y.E.; Park, J.H. Stem Electrical Conductivity of Broccoli (*Brassica oleracea* L. var. *italica Plenk*) Under Nitrogen and Phosphorus Fertilizer Deficiency. *Agronomy* **2026**, *16*, 778. [CrossRef]
38. Cseresnyés, I.; Takács, T.; Sepovics, B.; Kovács, R.; Füzy, A.; Parádi, I.; Rajkai, K. Electrical Characterization of the Root System: A Noninvasive Approach to Study Plant Stress Responses. *Acta Physiol. Plant.* **2019**, *41*, 169. [CrossRef]
39. Bonetti, S.; Breitenstein, D.; Fatichi, S.; Domec, J.-C.; Or, D. Persistent decay of fresh xylem hydraulic conductivity varies with pressure gradient and marks plant responses to injury. *Plant Cell Environ.* **2021**, *44*, 371–386. [PubMed]
40. Savi, T. Plant hydraulics and measurement of vulnerability to embolism formation: A guide for beginners. *Die Bodenkult.* **2023**, *74*, 71–81. [CrossRef]
41. Konrad, W.; Katul, G.; Roth-Nebelsick, A.; Jensen, K.H. Xylem functioning, dysfunction and repair: A physical perspective and implications for phloem transport. *Tree Physiol.* **2019**, *39*, 184–201.
42. Bard, A.J.; Faulkner, L.R. *Electrochemical Methods: Fundamentals and Applications*, 2nd ed.; Wiley: Hoboken, NJ, USA, 2001.
43. Huang, Z.; Jiang, W.; Zhou, X.; Wang, B.; Ji, H.; Li, H. A New Method of Capacitively Coupled Contactless Conductivity Detection Based on Series Resonance. *Sens. Actuators B Chem.* **2009**, *143*, 239–245. [CrossRef]
44. Yang, M.P.; Wang, C.F.; Cai, J.; Lai, X.C.; Cao, M.Y.; Zhao, X.Q. Advancement of Microchip Electrophoresis Coupled with Capacitively Coupled Contactless Conductivity Detection—From Design to Application (2018–2024). *Anal. Sci.* **2025**, *41*, 903–921. [CrossRef] [PubMed]
45. Kubán, P.; Hauser, P.C. Contactless Conductivity Detection for Analytical Techniques: Developments from 2016 to 2018. *Electrophoresis* **2019**, *40*, 124–139. [PubMed]
46. Hauser, P.C.; Kubán, P. Contactless Conductivity Detection for Capillary Electrophoresis—Developments from 2020 to 2024. *Electrophoresis* **2025**, *46*, 829–862. [PubMed]
47. Huang, J.; Jiang, Y.; Ji, H.; Wang, B.; Huang, Z. Electrical Impedance Characteristics of Slug Flow in Small Channels and Its Application to Void Fraction Estimation. *Int. J. Multiph. Flow* **2022**, *156*, 104200. [CrossRef]

48. Ye, X.; Wang, Y.; Tang, X.-Y.; Ji, H.; Wang, B.; Huang, Z. On the Design of a New Simulated Inductor Using a Contactless Electrical Tomography System as an Example. *Sensors* **2019**, *19*, 2568. [CrossRef]
49. Wang, C.; Huang, J.; Ji, H.; Wang, B.; Huang, Z. A New Gas Slug Length Measurement Method of Slug Flow in Small Channels Based on a Contactless Impedance Detection Sensor. *Flow Meas. Instrum.* **2025**, *106*, 102345. [CrossRef]
50. Huang, J.; Sheng, B.; Ji, H.; Huang, Z.; Wang, B.; Li, H. A New Contactless Bubble/Slug Velocity Measurement Method of Gas-Liquid Two-Phase Flow in Small Channels. *IEEE Trans. Instrum. Meas.* **2019**, *68*, 3253–3267. [CrossRef]
51. Bezdek, J.C. Cluster Validity with Fuzzy Sets. *J. Cybern.* **1974**, *3*, 58–73.
52. Sergios, T. *Pattern Recognition*; Elsevier: Singapore, 2012.
53. Del Zozzo, F.; Canavera, G.; Frioni, T.; Magnanini, E.; Poni, S. A novel low-cost trunk load cell sensor for estimating canopy transpiration in the grapevine. *Agric. Water Manag.* **2025**, *312*, 109432. [CrossRef]
54. Villalobos, F.J.; Testi, L.; García-Tejera, O.; López-Bernal, A.; Tejada, I.; Vinagre, B.M. Measuring the Diurnal Variation of Root Conductance in Olive Trees Using Microtensiometers and Sap Flow Sensors. *Plant Soil* **2025**, *509*, 999–1012.
55. Nieto, L.G.; Huber, A.; Gao, R.; Biasuz, E.C.; Cheng, L.L.; Stroock, A.D.; Lakso, A.N.; Robinson, T.L. Trunk Water Potential Measured with Microtensiometers for Managing Water Stress in "Gala" Apple Trees. *Plants* **2023**, *12*, 1912. [CrossRef]
56. Blanco, V.; Kalcsits, L. Microtensiometers Accurately Measure Stem Water Potential in Woody Perennials. *Plants* **2021**, *10*, 2780. [CrossRef] [PubMed]
57. Mancha, L.A.; Uriarte, D.; Prieto, M.d.H. Characterization of the Transpiration of a Vineyard under Different Irrigation Strategies Using Sap Flow Sensors. *Water* **2021**, *13*, 2867. [CrossRef]
58. Forster, M.A. The Dual Method Approach (DMA) Resolves Measurement Range Limitations of Heat Pulse Velocity Sap Flow Sensors. *Forests* **2019**, *10*, 46. [CrossRef]
59. Teramoto, M.; Shi, L.; Seimiya, N.; Takei, K. Minimally Invasive Multimodal Flexible Sensors to Monitor Stem Growth Rate, Soil Water Content, and Soil pH. *ACS Sens.* **2025**, *10*, 6195–6205. [CrossRef] [PubMed]
60. Yogi, P.; Pawar, A.D.; Khaparde, P.; Garg, P.; Kalita, H.; Palaparthy, V.S. Detection of Small Water Droplets on Flexible Leaf Wetness Sensor Considering the Effect of Spatiotemporal Variation. *IEEE Sens. J.* **2025**, *25*, 33540–33547. [CrossRef]
61. Xu, Q.; Li, J.; Zhang, Y.; Wang, J.; Liang, T.; Wang, A.; Liaoyang, Z.; Guo, W.; Cheng, X. Early in-situ detection of tobacco root diseases using a wearable plant sensor. *Ind. Crops Prod.* **2025**, *237*, 122090. [CrossRef]